Time-domain extended-reaction microperforated panel sound absorber modeling for acoustics simulation by finite element method

Yoshida, Takumi
Okuzono, Takeshi
Sakagami, Kimihiro

(Citation)
Acoustical Science and Technology,45(2):57-68

(Issue Date)
2024-03-01

(Resource Type)
journal article

(Version)
Version of Record

Acoust. Sci. & Tech. **45**, 2 (2024)

PAPER

Time-domain extended-reaction microperforated panel sound absorber modeling for acoustics simulation by finite element method

Takumi Yoshida, Takeshi Okuzono* and Kimihiro Sakagami

Environmental Acoustic Laboratory, Department of Architecture, Graduate School of Engineering, Kobe University, 1–1 Rokkodai-cho, Nada-ku, Kobe, 657–8501 Japan

(*Received 25 March 2023, Accepted for publication 7 September 2023*)

Abstract: For precise wave-based room acoustics modeling, an accurate extended-reaction (ER) sound absorber model must be formulated to assess frequency and incident-angle dependences of a sound absorber. Two novel efficient time-marching schemes with implicit time-domain FEM (TD-FEM) are presented to model the extended reacting boundary of microperforated panel (MPP) sound absorbers. Generally, MPP absorbers (MPPAs) have an air cavity behind them, which causes ER behavior. Formulating the ER behavior of MPPAs is necessary for simulating room acoustics. A hindrance to the time-domain modeling of the ER of MPPAs is the need to treat its complex impedance on the microperforations. The proposed schemes model MPPs as interior boundary conditions and deal with the complex transfer impedance with auxiliary differential equations (ADEs), producing stable schemes after the Crank–Nicolson solver is applied. For scheme verification, the impedance tube model with a single-leaf MPPA is analyzed. Additionally, the effectiveness of the proposed schemes is assessed by practical room acoustics modeling involving MPPAs and comparison with a frequency-domain FEM solver, which can address complex transfer impedance exactly. The results show excellent performance of the proposed methods. The TD-FEMs can model room acoustics, including the MPPA, $\mathcal{O}(100)$ times faster while maintaining accuracy comparable to that of FD-FEM.

Keywords: Extended reaction, Microperforated panel absorber, Time-domain FEM, Wave-based room-acoustics simulation

1. INTRODUCTION

Wave-based room acoustics simulation using the finite element method (FEM) attracts intense interest because of its high flexibility for boundary shape modeling. Recently, by virtue of the development of highly efficient solvers with a sound-absorbing boundary considering the frequency-dependent complex-valued surface impedance of sound-absorbing materials, it is becoming possible to apply time-domain finite element method (TD-FEM)-based numerical solvers to the broadband acoustic modeling of realistic rooms [1–7]. However, for more precise simulations of room acoustics, it is crucially important to use extended-reaction (ER) sound-absorbing models able to incorporate both the frequency and incident-angle dependences of absorbing materials. Generally, constructing TD-ER models for various sound absorbers is a considerably difficult task because it requires a solution of additional ordinary differential equations with complicated frequency-dependent parameters such as complex wavenumbers and complex effective density.

Frequency-domain FEM (FD-FEM) solvers have greater capabilities for using ER models for various sound absorbers because they can deal naturally with frequency-dependent parameters. For example, porous materials have been modeled using absorption finite elements based on the equivalent fluid model (EFM) [8–14]. Additionally, thin materials such as permeable membranes and microperforated panels (MPPs) have been modeled with interior impedance boundary conditions [15–17]. Nevertheless, recent work [6] has demonstrated that TD-FEM has benefits for computational times for large-scale problems such as real-sized 3D room acoustics simulation. Therefore, developing a TD-ER model for TD-FEM to realize high-efficiency wave-based room acoustics simulation is an attractive topic.

In some recent works, a time-domain ER formulation on porous absorbers, such as glass wool and thin fabrics, that is equivalent to the frequency-domain formulations has been examined. A general formulation of the time-domain EFM to address porous materials for TD-FEM, which

*e-mail: okuzono@port.kobe-u.ac.jp
[doi:10.1250/ast.e23.16]

solves the TD expression of the Helmholtz equation with a complex wavenumber, was proposed in earlier work [18]. In this formulation, convolutions involving two frequency-dependent parameters, complex wavenumber, and complex effective density were processed efficiently by an auxiliary differential equation (ADE) method [19]. By the ADE method, the direct convolution is converted to a bunch of ordinary differential equations solved with small computational effort. For the TD discontinuous Galerkin FEM (TD-DGFEM), EFM is also available with the same concept, by which a set of first-order partial differential equations of porous materials is solved by the ADE method [20,21]. For permeable membranes, the TD-ER model was implemented efficiently into implicit and explicit TD-FEMs [22,23] and TD-DGFEM [21] on the basis of the interior impedance boundary conditions with frequency-independent flow resistance and surface density.

However, efficient TD-ER models for resonant absorbers, such as MPP absorbers, have not been developed. Because resonant absorbers show strong incident-angle-dependent sound absorption with backing air space, their development is of crucial importance.

As another approach, a phenomenological ER boundary model assuming sparse reflection conditions has been reported [24]. This approach can model the ER of any sound absorber by imposing surface impedance at each angle upon identifying the incident angle of sound by a wave-splitting method. However, it is feasible only in early sound fields in large rooms. Additionally, this modeling requires the intensive usage of large amounts of memory to store the surface impedance at numerous incident angles for assigned materials. Consequently, a robust and efficient ER model of resonant absorbers must be developed.

Among resonant absorbers, the analyses presented in this paper explicitly address an ER model for MPP absorbers, which consist of the local-reaction perforated panel and ER back structure. The MPP absorbers are highly attractive because of their prominent designability and sound absorptivity derived from micro sized holes. The proposed ER model is based on interior impedance boundary conditions with frequency-dependent transfer admittance, a time-domain counterpart of the frequency-domain model proposed in an earlier report [16], and an extension of the TD-ER model of permeable membranes [22]. We also describe the specific implementation procedure of the present time-domain ER model of MPP absorbers into an implicit TD-FEM formulation [3–6] for room-acoustics simulation. The point of novelty of the present work is that this report is the first to propose a general formulation of the implicit TD-FEM dealing with a time-domain ER model of MPP absorbers. Any finite element type for spatial discretization can be used for the formulation. Moreover, if the ADE method performs well, the present ER model will be useful for other resonant absorbers with different transfer impedance models.

In this paper, we first present two novel formulations of implicit TD-FEM schemes for acoustics simulation, including MPP sound absorbers. Assisted by the ADE method, the new schemes address the frequency-dependent transfer impedance of a rigid or limp MPP. Our proposals have high stability owing to the use of the Crank–Nicolson method to solve a set of first-order ordinary differential equations in the ADE method. Firstly, the two proposed schemes are verified via impedance tube problems with a single-leaf MPP absorber. Then, the higher efficiency of the proposed schemes against existing frequency-domain solvers is demonstrated via small-room acoustics simulation including single-leaf MPP absorbers.

2. GENERAL FORMULATION OF TD-FEM INCORPORATED WITH A TIME-DOMAIN ER MODEL OF MPP ABSORBERS

In this section, we present two possible general formulations to address the ER of MPP sound absorbers in TD-FEM [3,4,6] for acoustics simulation. For simplicity, we describe only the relevant theory with the ER of MPP sound absorbers. Earlier reports [3,4,6] include detailed formulations of TD-FEM.

2.1. Interior Impedance Boundary Conditions for MPP

In this study, we model the ER of MPP absorbers with interior impedance boundary conditions. With the boundary conditions, the MPP leaf itself is modeled by a thin and limp membrane having transfer admittance Y_{LM} as a local-reaction material, but it can couple with a sound field behind the MPP leaf. The conditions enable the modeling of the incident-angle dependence of the specific acoustic impedance of MPP absorbers relevant to acoustic wave propagation inside MPP absorbers. The transfer admittance Y_{t} is defined as [25]

$$Y_{\mathrm{t}} = \left(\frac{1}{\mathrm{j}\omega M_{\mathrm{M}}} + Y_{\mathrm{M}} \right), \tag{1}$$

where M_{M} is the MPP surface density and Y_{M} is the transfer admittance for a rigid MPP. j and ω respectively denote the imaginary unit $\sqrt{-1}$ and the angular frequency. The analyses presented herein use Maa's [26] transfer admittance model of MPPs as

$$Y_{\mathrm{M}} = \frac{\sigma}{R_0 + \mathrm{j}I_0}, \tag{2}$$

where

$$R_0 = \frac{32\eta t}{d^2} \left(\sqrt{1 + \frac{K^2}{32}} + \frac{\sqrt{2}}{8} K \frac{d}{t} \right), \tag{3}$$

$$I_0 = \rho_0 \omega t \left(1 + \frac{1}{\sqrt{9 + K^2/2}} + 0.85 \frac{d}{t} \right), \tag{4}$$

$$K = d \sqrt{\frac{\omega \rho_0}{4\eta}}. \tag{5}$$

Therein, σ, t, d, and η respectively signify the perforation rate, the MPP thickness, the hole diameter, and the dynamic viscosity of air (17.9 μPa s). Also, ρ_0 represents the air density. Other impedance models of MPP are available to Y_{M} for use instead of the classical Maa model.

With transfer admittance, an interior impedance boundary condition is imposed for both sides of an MPP, $\Gamma_{\mathrm{MPP,a}}$ and $\Gamma_{\mathrm{MPP,b}}$, as

$$\frac{\partial p}{\partial n} = \begin{cases} -Y_{\mathrm{LM}} \Delta p & \text{on } \Gamma_{\mathrm{MPP,a}}, \\ Y_{\mathrm{LM}} \Delta p & \text{on } \Gamma_{\mathrm{MPP,b}}, \end{cases} \tag{6}$$

with

$$Y_{\mathrm{LM}} = \mathrm{j}\omega Y_{\mathrm{t}}, \tag{7}$$

where Δp represents the sound pressure difference between the two sides of an MPP. In FD-FEM formulation [16,17], incorporating the interior impedance boundary condition above into the Helmholtz equation yields the following discretized matrix equation:

$$(c_0^2 \boldsymbol{K} - \omega^2 \boldsymbol{M} \boldsymbol{p} + \rho_0 c_0^2 Y_{\mathrm{LM}} \boldsymbol{S}) \boldsymbol{p} = \boldsymbol{f}. \tag{8}$$

Therein, $\boldsymbol{M}$ and $\boldsymbol{K}$ respectively denote the global mass and the global stiffness matrices. Furthermore, $\boldsymbol{S}$ stands for the global matrix to the contribution of an MPP. $\boldsymbol{p}$ and $\boldsymbol{f}$ respectively represent the sound pressure and external force vectors. As shown later, both Y_{M} and Y_{LM} are complex frequency-dependent functions (see Fig. 1). Consequently, the TD form of Eq. (8) involves convolution integrals. The analyses described herein cope efficiently with the convolution by the ADE method.

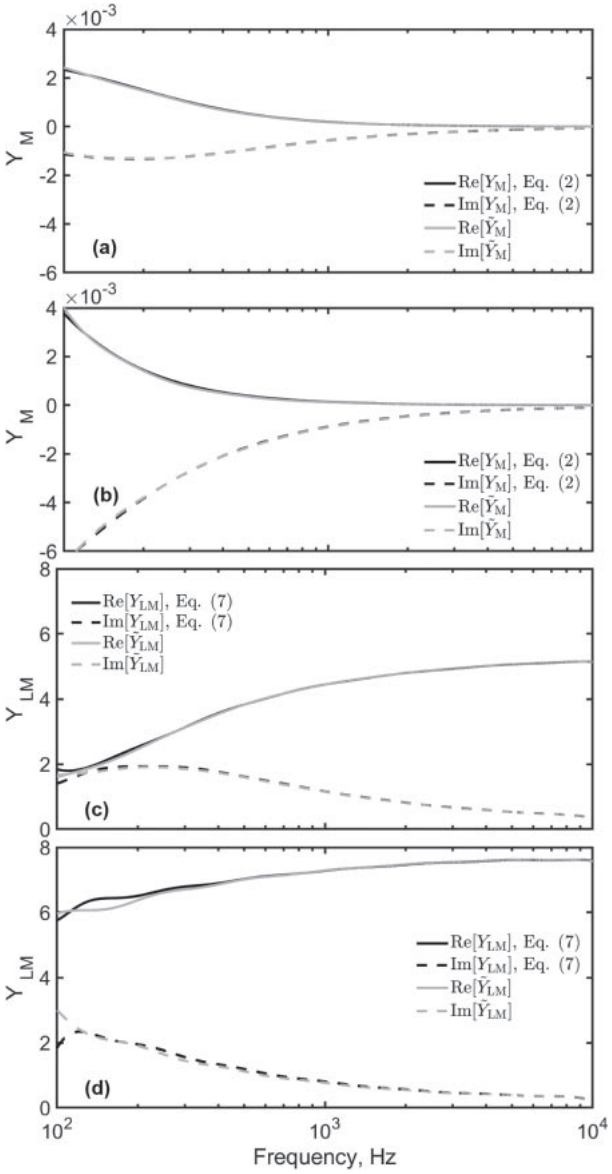

Fig. 1 Theoretical values of Y_{M} and Y_{LM}, and the rational function values of $\tilde{Y}_{\mathrm{M}}$ and $\tilde{Y}_{\mathrm{LM}}$. (a) MPP 1: Y_{M} vs. $\tilde{Y}_{\mathrm{M}}$, (b) MPP 2: Y_{M} vs. $\tilde{Y}_{\mathrm{M}}$, (c) MPP 1: Y_{LM} vs. $\tilde{Y}_{\mathrm{LM}}$, and (d) MPP 2: Y_{LM} vs. $\tilde{Y}_{\mathrm{LM}}$.

2.2. Time-Marching Schemes

Two possible time-marching schemes of the implicit TD-FEM with MPP absorbers are formulated here because it remains unclear which formulation is more accurate and efficient. Two possible time-domain forms of Eq. (8) exist, as obtained from an inverse Fourier transformation with a time factor of $\exp(\mathrm{j}\omega t)$:

$$\boldsymbol{M} \ddot{\boldsymbol{p}} + c_0^2 \boldsymbol{K} \boldsymbol{p} + \frac{\rho_0 c_0^2}{M_{\mathrm{M}}} \boldsymbol{S} \boldsymbol{p} + \rho_0 c_0^2 \boldsymbol{S} [\hat{Y}_{\mathrm{M}} * \dot{\boldsymbol{p}}] = \boldsymbol{f}, \tag{9}$$

and

$$\boldsymbol{M} \ddot{\boldsymbol{p}} + c_0^2 \boldsymbol{K} \boldsymbol{p} + \rho_0 c_0^2 \boldsymbol{S} [\hat{Y}_{\mathrm{LM}} * \boldsymbol{p}] = \boldsymbol{f}. \tag{10}$$

Therein, $\hat{Y}_{\mathrm{M}}$ and $\hat{Y}_{\mathrm{LM}}$ respectively denote the inverse Fourier-transformed values of Y_{M} and Y_{LM}. The difference between them is that Eq. (10) involves the mass reactance term of MPPs in Eq. (9) in the convolution integrals. The second time-domain expression of Eq. (10) is beneficial because the fully explicit formulation is possible using the explicit TD-FEM formulation [5,7]. Hereinafter, the time-marching schemes based on Eqs. (9) and (10) are designated as Schemes 1 and 2, respectively.

2.2.1. Scheme 1

In the first time-marching scheme, the convolution integral $\hat{Y}_{\mathrm{M}} * \dot{\boldsymbol{p}}$ in Eq. (9) is approximated to the following rational function form of Y_{M} according to the ADE method [19]:

$$Y_{\mathrm{M}}(\omega) \approx \tilde{Y}_{\mathrm{M}}(\omega) = Y_{\mathrm{M}\infty} + \sum_{i=1}^{n_{\mathrm{rp}}} \frac{A_i}{\lambda_i + \mathrm{j}\omega} + \sum_{i=1}^{n_{\mathrm{cp}}} \left(\frac{B_i - \mathrm{j}C_i}{\alpha_i - \mathrm{j}\beta_i + \mathrm{j}\omega} + \frac{B_i + \mathrm{j}C_i}{\alpha_i + \mathrm{j}\beta_i + \mathrm{j}\omega} \right). \quad (11)$$

In those expressions, n_{rp} and n_{cp} represent the quantities of real poles λ_i and pairs of complex conjugate poles $\alpha_i \pm \beta_i$. $Y_{\mathrm{M}\infty}$, A_i, B_i and C_i are real parameters. To maintain causality, $\lambda_i \geq 0$ and $\alpha_i \geq 0$ is demanded. In addition, $\mathrm{Re}(\tilde{Y}_{\mathrm{M}}(\omega)) \geq 0$ is kept for ensuring passivity. Then, with the rational function form, the convolution in Eq. (9) is approximated as

$$\hat{Y}_{\mathrm{M}} * \dot{\boldsymbol{p}} \approx Y_{\mathrm{M}\infty}\dot{\boldsymbol{p}} + \sum_{i=1}^{n_{\mathrm{rp}}} A_i \boldsymbol{\phi}_i + 2\sum_{i=1}^{n_{\mathrm{cp}}} (B_i \boldsymbol{\psi}_i^{(1)} + C_i \boldsymbol{\psi}_i^{(2)}), \quad (12)$$

where $\boldsymbol{\phi}$, $\boldsymbol{\psi}^{(1)}$, and $\boldsymbol{\psi}^{(2)}$ are accumulator vectors, which are represented as

$$\begin{aligned} \dot{\boldsymbol{\phi}}_i + \lambda_i \boldsymbol{\phi}_i &= \dot{\boldsymbol{p}}, \\ \dot{\boldsymbol{\psi}}_i^{(1)} + \alpha_i \boldsymbol{\psi}_i^{(1)} + \beta_i \boldsymbol{\psi}_i^{(2)} &= \dot{\boldsymbol{p}}, \\ \dot{\boldsymbol{\psi}}_i^{(2)} + \alpha_i \boldsymbol{\psi}_i^{(2)} - \beta_i \boldsymbol{\psi}_i^{(1)} &= \boldsymbol{0}. \end{aligned} \quad (13)$$

In the rational function model, the conjugate complex pole pair term models the resonance in admittance. However, both Y_{M} and Y_{LM} have no resonance, as shown in Fig. 1. Eventually, $\tilde{Y}_{\mathrm{M}}$ can be approximated with only real poles. Hereinafter, we omit from the formulation those terms associated with complex poles. This is also true for Scheme 2 using $\hat{Y}_{\mathrm{LM}}$. With Eq. (12), Eq. (9) is transformed into

$$\boldsymbol{M}\ddot{\boldsymbol{p}} + c_0^2 \left(\boldsymbol{K} + \frac{\rho_0}{M_{\mathrm{M}}} \boldsymbol{S} \right) \boldsymbol{p} + \rho_0 c_0^2 Y_{\mathrm{M}\infty} \boldsymbol{S}\dot{\boldsymbol{p}} + \rho_0 c_0^2 \boldsymbol{S} \sum_{i=1}^{n_{\mathrm{rp}}} A_i \boldsymbol{\phi} = \boldsymbol{f}. \quad (14)$$

To solve the above semidiscrete equation in the temporal domain, we apply the fourth-order accurate Fox–Goodwin method to Eq. (14) and the unconditionally stable Crank–Nicolson method to Eq. (13). That time discretization yields the following time-marching scheme presented as Scheme 1:

$$\begin{aligned} &\left(\boldsymbol{M} + \frac{c_0^2 \Delta t^2}{12} \left(\boldsymbol{K} + \frac{\rho_0}{M_{\mathrm{M}}} \boldsymbol{S} \right) + \frac{\Delta t}{2} \rho_0 c_0^2 Y_{\mathrm{M}\infty} \boldsymbol{S} \right) \ddot{\boldsymbol{p}}^{n+1} \\ &= \boldsymbol{f}^{n+1} - c_0^2 \left(\boldsymbol{K} + \frac{\rho_0}{M_{\mathrm{M}}} \boldsymbol{S} \right) \boldsymbol{Q}^n \\ &\quad - \rho_0 c_0^2 Y_{\mathrm{M}\infty} \boldsymbol{S} \boldsymbol{P}^n - \rho_0 c_0^2 \boldsymbol{S} \sum_{i=1}^{n_{\mathrm{rp}}} A_i \boldsymbol{\phi}_i^{n+1}, \end{aligned} \quad (15)$$

$$\boldsymbol{p}^{n+1} = \boldsymbol{p}^n + \Delta t \dot{\boldsymbol{p}}^n + \Delta t^2 \left(\frac{5}{12} \ddot{\boldsymbol{p}}^n + \frac{1}{12} \ddot{\boldsymbol{p}}^{n+1} \right), \quad (16)$$

$$\dot{\boldsymbol{p}}^{n+1} = \dot{\boldsymbol{p}}^n + \frac{\Delta t}{2} (\ddot{\boldsymbol{p}}^n + \ddot{\boldsymbol{p}}^{n+1}), \quad (17)$$

with

$$\boldsymbol{P}^n = \dot{\boldsymbol{p}}^n + \frac{\Delta t}{2} \ddot{\boldsymbol{p}}^n, \quad (18)$$

$$\boldsymbol{Q}^n = \boldsymbol{p}^n + \Delta t \dot{\boldsymbol{p}}^n + \frac{5\Delta t^2}{12} \ddot{\boldsymbol{p}}^n, \quad (19)$$

$$\boldsymbol{\phi}_i^{n+1} = \frac{\Delta t}{2 + \lambda_i \Delta t} \left(\frac{\Delta t}{2} \ddot{\boldsymbol{p}}^{n+1} + \boldsymbol{P}^n \right) + \boldsymbol{X}^{n+1}, \quad (20)$$

$$\boldsymbol{X}^{n+1} = \frac{(2 - \lambda_i \Delta t)\boldsymbol{\phi}_i^n + \Delta t \dot{\boldsymbol{p}}^n}{2 + \lambda_i \Delta t}. \quad (21)$$

As the linear equation solver of Eq. (15), the conjugate gradient (CG) solver with a diagonal scaling preconditioning is used with a convergence tolerance of 10^{-4}. In comparison with the case without MPPs, the scheme has an additional memory requirement for storing the matrix $\boldsymbol{S}$ and the accumulator vectors, and an additive computational complexity per iteration for the matrix-vector products in the third and fourth terms of the right-hand side of Eq. (15) and the time-marching computation of the accumulators. However, those differences are generally small because the surface area of installed MPPs is much less than the room volume.

2.2.2. Scheme 2

The second time-marching scheme uses the following rational function form of Y_{LM} as

$$Y_{\mathrm{LM}}(\omega) \approx \tilde{Y}_{\mathrm{LM}}(\omega) = Y_{\mathrm{L}\infty} + \sum_{i=1}^{n_{\mathrm{rp}}} \frac{A_i'}{\lambda_i' + \mathrm{j}\omega}. \quad (22)$$

The parameter λ_i' is the real pole. In that equation, $Y_{\mathrm{L}\infty}$ and A_i' are the real-valued coefficients. Using the rational function form $\tilde{Y}_{\mathrm{LM}}$, the convolution in Eq. (10) is approximated as

$$\hat{Y}_{\mathrm{LM}} * \boldsymbol{p} \approx Y_{\mathrm{L}\infty}\boldsymbol{p} + \sum_{i=1}^{n_{\mathrm{rp}}} A_i' \boldsymbol{\phi}_i'. \quad (23)$$

The accumulator $\boldsymbol{\phi}'$ is given as

$$\dot{\boldsymbol{\phi}}_i' + \lambda_i' \boldsymbol{\phi}_i' = \boldsymbol{p}. \quad (24)$$

Using Eq. (23), the semidiscrete equation of Eq. (10) is approximated as

$$\boldsymbol{M}\ddot{\boldsymbol{p}} + c_0^2 \boldsymbol{K}\boldsymbol{p} + \rho_0 c_0^2 Y_{\mathrm{L}\infty} \boldsymbol{S}\boldsymbol{p} + \rho_0 c_0^2 \boldsymbol{S} \sum_{i=1}^{n_{\mathrm{rp}}} A_i' \boldsymbol{\phi}' = \boldsymbol{f}. \quad (25)$$

Similarly to Scheme 1, time discretization using the Fox–Goodwin method and the Crank–Nicolson method yields

$$\left(\boldsymbol{M}+\frac{c_0^2\Delta t^2}{12}(\boldsymbol{K}+\rho_0 Y_{\mathrm{L}\infty}\boldsymbol{S})\right)\ddot{\boldsymbol{p}}^{n+1}=\boldsymbol{f}^{n+1}$$

$$-c_0^2(\boldsymbol{K}+\rho_0 Y_{\mathrm{L}\infty}\boldsymbol{S})\boldsymbol{Q}^n-\rho_0 c_0^2\boldsymbol{S}\sum_{i=1}^{n_{\mathrm{rp}}}A_i'\boldsymbol{\phi}_i'^{n+1}, \quad (26)$$

with

$$\boldsymbol{\phi}_i'^{n+1}=\frac{\Delta t}{2+\lambda_i'\Delta t}\left(\frac{\Delta t^2}{12}\ddot{\boldsymbol{p}}^{n+1}+\boldsymbol{Q}^n\right)+\boldsymbol{X}'^{n+1}, \quad (27)$$

$$\boldsymbol{X}'^{n+1}=\frac{(2-\lambda_i'\Delta t)\boldsymbol{\phi}_i'^{n}+\Delta t\dot{\boldsymbol{p}}^n}{2+\lambda_i'\Delta t}. \quad (28)$$

The vectors $\boldsymbol{p}^{n+1}$ and $\dot{\boldsymbol{p}}^{n+1}$ are computed using Eqs. (16) and (17). The linear system equation of Eq. (26) is solved by the diagonal scaling preconditioned CG solver with a convergence tolerance of 10^{-4}. Scheme 2 has the same memory requirement as Scheme 1 but with a lower computational complexity per iteration because Eq. (26) does not have the matrix-vector product equivalent to the third term of the right-hand side of Eq. (15). Regarding spatial discretization, the two proposed schemes can use any type of finite element (FE), but in the work described by this paper, linear hexahedral elements with modified integration rules [27] are used for dispersion error reduction.

3. VERIFICATION WITH IMPEDANCE TUBE PROBLEM

We verify the two proposed schemes with a theoretical solution from the transfer matrix method (TMM) [28]. To this end, the sound absorption characteristics of single-leaf MPP absorbers at normal incidence were computed using Schemes 1 and 2, adopting an impedance tube problem. The results were compared with the theoretical results obtained from TMM [6]. Four MPP materials (MPP 1–MPP 4), each with different geometrical parameters, were tested. Table 1 shows four material parameters of MPPs: surface density, perforation ratio, plate thickness, and hole diameter. The backing air cavity depth of single-leaf MPP absorbers was 0.05 m. For Scheme 1, the respective transfer admittance $\tilde{Y}_{\mathrm{M}}$ values of MPP 1–MPP 4 were approximated by the rational function form with real poles $n_{\mathrm{rp}}=$ 11, 11, 11, and 14, respectively. By contrast, Scheme 2 uses the rational function form $\tilde{Y}_{\mathrm{LM}}$ with real poles $n_{\mathrm{rp}}=11$, 16, 16, and 18 for MPP 1–MPP 4, respectively. To achieve passively rational approximation, vector fitting [29] with passivity enforcement [30] was applied. The minimum number of poles was used to ensure that the root mean square error between the theoretical TMM and rational function approximation values does not decrease when the number of poles is varied. As a reference, Fig. 1 shows how the rational function forms $\tilde{Y}_{\mathrm{M}}$ and $\tilde{Y}_{\mathrm{LM}}$ fit the theoretical values of Y_{M} and Y_{LM} in Eqs. (2) and (7) for MPP 1 and MPP 2. The rational function forms $\tilde{Y}_{\mathrm{M}}$ for Scheme 1 show good agreement with theoretical transfer admittance at 100 Hz–10 kHz frequencies. Although $\tilde{Y}_{\mathrm{LM}}$ for Scheme 2 also generally shows good agreement with the theoretical values, some discrepancies are observed at low frequencies.

Table 1 Geometrical parameters of four MPPs: surface density M_{M}, perforation ratio σ, plate thickness t, and hole diameter d.

MPP	M_{M}, kg/m^2	σ, %	t, mm	d, mm
1	1.13	0.785	1	0.5
2	0.565	0.970	0.5	1
3	2.7	0.785	1	0.5
4	1.35	0.970	0.5	1

3.1. Simulation Outline

Figure 2 shows the impedance tube with a cross-sectional area of 0.01 m × 0.01 m to compute the complex reflection coefficient R, using Schemes 1 and 2. R was computed by the transfer function method [31]. Four single-leaf MPP absorbers with the four MPPs listed in Table 1 were mounted at a tube outlet with a rigid termination. The tube inlet was assigned two boundary conditions: a vibration boundary to emit the plane wave and an absorbing boundary with the characteristic impedance of air, $\rho_0 c_0$, for absorbing the reflected wave. A Gaussian pulse with an upper-limit frequency of 10 kHz was assigned to the vibration boundary as the vibration acceleration waveform. The tube model was spatially discretized with cubic FEs of 0.005 m element size, having a spatial resolution of 6.9 elements per wavelength at 10 kHz. Two microphones were placed at $(x, y, z) = (0.44, 0.005, 0.005)$ and $(0.45, 0.005, 0.005)$. Sound pressures up to 1.0 s were assessed under a time interval of 1/125,328 s, which was a 0.95 times stability limit value for acoustics simulation in lossless air domains. As presented in earlier work [22], the interior impedance boundary

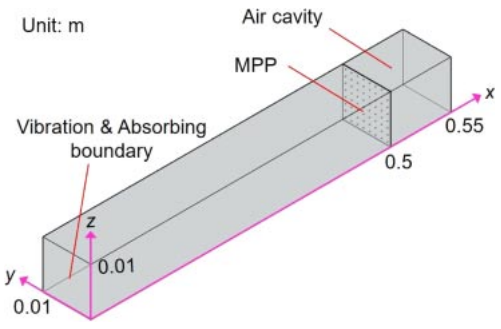

Fig. 2 Impedance tube model with a single-leaf MPP absorber.

condition introduces slightly worse stability, which is also true for the proposed schemes. However, because of the unconditionally stable Crank–Nicolson solver, our two proposed schemes do not introduce any additional stability reduction in the accumulator computations.

For the quantification of the accuracy of numerical results, we evaluated the relative L_2-norm errors of the amplitude and the phase vectors of R at frequencies [100, 10,000] Hz against the theoretical TMM and numerical results as

$$e_{\mathrm{a}} = \frac{\|\boldsymbol{R}_{\mathrm{a}} - \tilde{\boldsymbol{R}}_{\mathrm{a}}\|_2}{\|\boldsymbol{R}_{\mathrm{a}}\|_2}, \quad e_{\mathrm{p}} = \frac{\|\boldsymbol{R}_{\mathrm{p}} - \tilde{\boldsymbol{R}}_{\mathrm{p}}\|_2}{\|\boldsymbol{R}_{\mathrm{p}}\|_2}, \tag{29}$$

where $\boldsymbol{R}_{\mathrm{a}}$ and $\boldsymbol{R}_{\mathrm{p}}$ respectively represent the amplitude and phase vectors of the R calculated using TMM. $\tilde{\boldsymbol{R}}_{\mathrm{a}}$ and $\tilde{\boldsymbol{R}}_{\mathrm{p}}$ are those obtained using Schemes 1 and 2.

3.2. Results

Figure 3 shows the amplitudes of R of single-leaf MPP absorbers with MPP 1 and MPP 2 for theoretical TMM, TMM with the rational function values, and Schemes 1 and 2. We found that TMM with the rational function values matches well with theoretical TMM except for dip frequencies in some cases. For example, we can see slight discrepancies at the first resonant frequency in Figs. 3(b) and 3(d). This result suggests the necessity of a better fitting method. Schemes 1 and 2 qualitatively agree with theoretical TMM and agree better with TMM with the rational function values, demonstrating that the two schemes can at least capture the rational function values. MPP 3 and MPP 4 respectively showed the same tendencies as MPP 1 and MPP 2.

Figure 4 shows the phases of R for MPP 1 and MPP 2 using theoretical TMM, TMM with the rational function values, and the two schemes. We can find that the results of TMM with the rational function values and the two schemes generally agree with those of theoretical TMM, suggesting the validity of two proposed schemes. In Fig. 4(b), TMM with the rational function values shows a slight discrepancy from theoretical TMM at the third resonant frequency. This result also suggests the necessity of a better fitting method.

For a quantitative evaluation, Table 2 shows e_{a} and e_{p} in Schemes 1 and 2 for MPP 1–MPP 4. For the amplitude, Scheme 2 exhibits a slightly smaller error than Scheme 1, but they have almost the same level of accuracy. Also, e_{a} values of MPP 2 and 4 are larger than those of MPP 1 and 3, as expected. It might be expected that the proposed schemes have a larger error for MPP sound absorbers with R of larger value in magnitude at the first resonant frequency. On the other hand, Schemes 1 and 2 show almost the same degree of error in the phase, except for MPP 1. Scheme 1 shows much a lower e_{p} for MPP 1 than

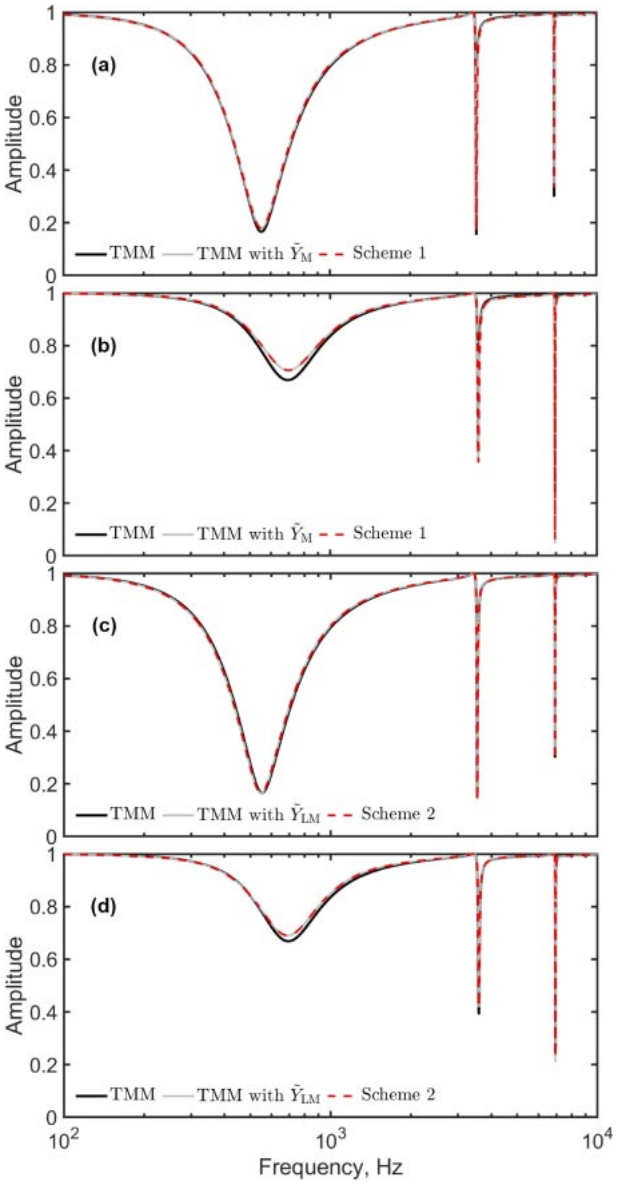

Fig. 3 Amplitudes of R for TMM, TMMs with $\tilde{Y}_{\mathrm{M}}$ or $\tilde{Y}_{\mathrm{LM}}$, and Schemes 1 or 2: (a) MPP 1 (Scheme 1), (b) MPP 2 (Scheme 1), (c) MPP 1 (Scheme 2), and (d) MPP 2 (Scheme 2).

Scheme 2, but this is because the difference in phase between TMM and TMM with $\tilde{Y}_{\mathrm{M}}$ is very small. As a reference, e_{a} and e_{p} between TMM and TMMs with $\tilde{Y}_{\mathrm{M}}$ or $\tilde{Y}_{\mathrm{LM}}$ are shown in Table 3. The error level are comparable to those of the two schemes.

4. PERFORMANCE COMPARISON WITH FD-FEM SOLVER

In this section, we present the examination of the performance of the two proposed schemes compared with an existing FD-FEM solver [16] for a real-scale small-room acoustics problem. We test whether the two schemes produce a level of accuracy similar to that obtained by FD-FEM under using the same FE mesh while maintaining a

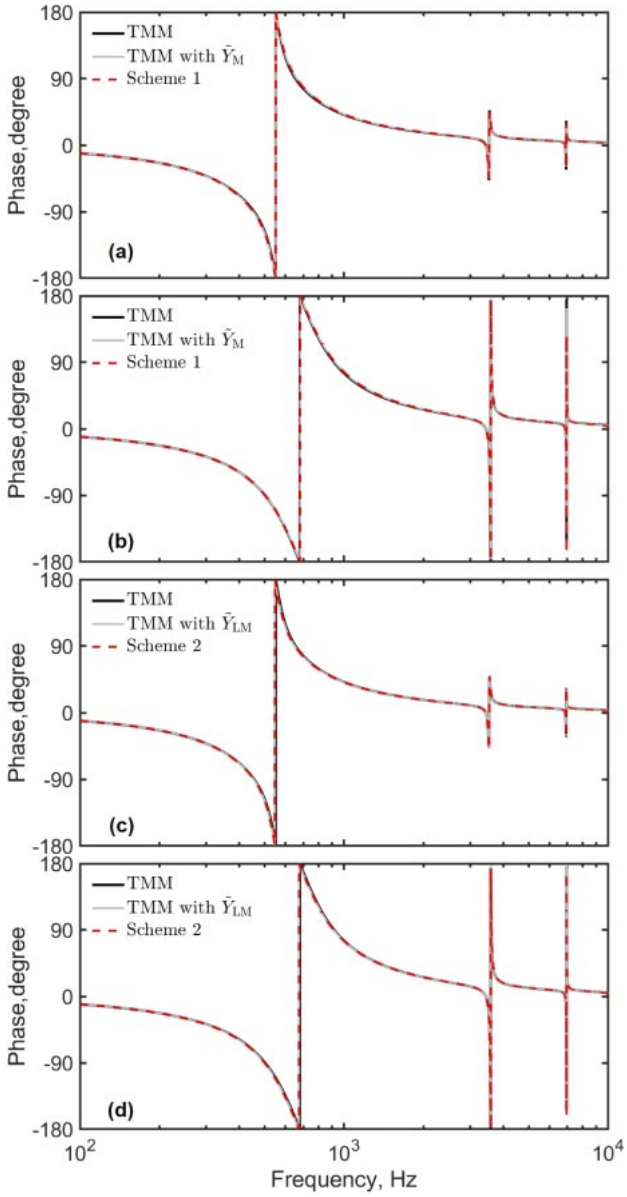

Fig. 4 Phases of R for TMM, TMMs with $\tilde{Y}_M$ or $\tilde{Y}_{LM}$, and Schemes 1 or 2: (a) MPP 1 (Scheme 1), (b) MPP 2 (Scheme 1), (c) MPP 1 (Scheme 2), and (d) MPP 2 (Scheme 2).

Table 2 e_a and e_p in Schemes 1 and 2 for each MPP.

MPP	e_a		e_p	
	Scheme 1	Scheme 2	Scheme 1	Scheme 2
1	0.0058	0.0042	0.0372	0.2772
2	0.0117	0.0062	0.2545	0.2778
3	0.0052	0.0051	0.2545	0.2778
4	0.0136	0.0073	0.2545	0.2778

higher computational efficiency. Earlier work [6] included a similar test, showing the higher efficiency of the baseline implicit TD-FEM without the interior impedance boundary conditions of MPPs. We compare the transfer functions

Table 3 e_a and e_p between TMM and TMM with $\tilde{Y}_M$ or $\tilde{Y}_{LM}$.

MPP	e_a		e_p	
	$\tilde{Y}_M$	$\tilde{Y}_{LM}$	$\tilde{Y}_M$	$\tilde{Y}_{LM}$
1	0.0048	0.0034	0.0276	0.2765
2	0.0116	0.0055	0.2328	0.2220
3	0.0043	0.0048	0.1666	0.3466
4	0.0131	0.0066	0.2951	0.2624

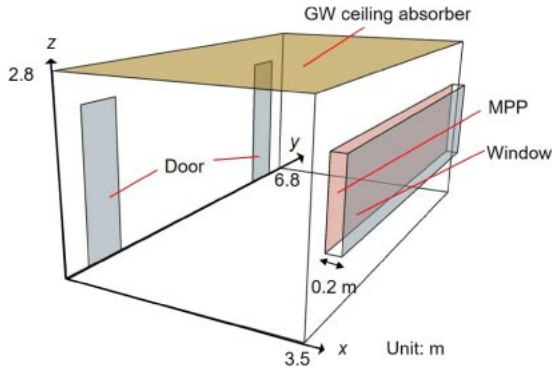

Fig. 5 Meeting room model with single-leaf MPP absorber and glass wool ceiling absorber.

and four room-acoustics parameters for examinations of accuracy.

Figure 5 presents a meeting room model of 68 m^3 for acoustics simulation, including a single-leaf MPP absorber in front of a window with 0.2 m air space and a glass wool (GW) ceiling absorber of 25 mm thickness. We consider MPP 1 and MPP 2 in Table 1. For this study, we used a supercomputer system at Kyushu University: ITO, Subsystem A, Fujitsu Primergy CX2550/CX2560M4 (Xeon Gold 6154 (3.0 GHz) $\times 2$ per node; Intel Corp.) and Fortran compiler (ver. 2020; Intel Corp.). Only a single node with 36 cores was used to perform parallel computations using OpenMP.

4.1. Simulation Outline

We computed an impulse response or a transfer function at frequencies up to the upper-limit frequency of the 1 kHz octave band using FD-FEM, Scheme 1, and Scheme 2. The meeting room was spatially discretized using cubic elements of 0.05 m edge size, such that the resulting mesh has a spatial resolution of 4.91 elements per wavelength at 1.4 kHz.

The GW ceiling absorber was modeled using a frequency-dependent impedance boundary condition with surface impedance computed using TMM. A one-parameter model called the Miki model [32] was used to compute the fluid properties of GW with a flow resistivity of 55,000 Pa s/m^2. The rational function form is presented in Table A3 of [4], where eight real poles and three complex

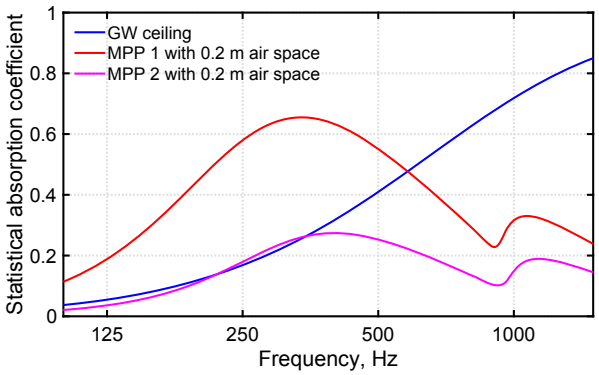

Fig. 6 Statistical absorption coefficients for the GW ceiling, MPP 1 with 0.2 m air space, and MPP 2 with 0.2 m air space.

poles were used. As a reference, the statistical absorption coefficients of the GW ceiling absorber and the two single-leaf MPP absorbers with MPP 1 and 2 are shown in Fig. 6. The two MPP absorbers have a peak sound absorption of approximately 250 Hz–500 Hz. Actually, MPP 1 shows the largest sound absorption below 500 Hz among the three sound absorbers and the primary sound absorber for low-frequency sound absorption. MPP 2 has an almost identical sound absorption below 350 Hz as the GW ceiling, which is the main absorber at frequencies higher than 500 Hz. The doors and the window were modeled using a frequency-independent impedance boundary condition with the real-valued acoustic admittance corresponding to a random incidence absorption coefficient of 0.05. Other boundaries were modeled using real-valued acoustic admittance corresponding to a random incidence absorption coefficient of 0.08. A source point was located at $(x, y, z) = (2.5, 5.8, 1.5)$. Eight receivers (R1–R8) were placed at the locations shown in Table 4.

As a sound source signal for time-domain simulation, Schemes 1 and 2 used the impulse response of an optimized FIR filter designed with the Parks–McClellan algorithm; it has a flat spectrum at 70 Hz–1.5 kHz. The impulse responses were calculated at the eight receivers with $\Delta t = 1/13{,}000$ s. The results were converted to the transfer function via the discrete Fourier transformation, canceling the sound source's characteristic. The FD-FEM computes transfer functions at 1 Hz–1.6 kHz with a 1 Hz interval using a volume acceleration of 1 m^3/s^2 for source excitation. The wider frequency range than the time-domain simulations is for causal inverse Fourier transformation. Two linear equation solvers were tested to solve Eq. (8): a sparse direct solver called PARDISO and an iterative solver called CSQMOR [33] with a convergence tolerance of 10^{-4}. As in earlier works [4,6], we examined the two solver's performance characteristics because an efficient solver in FD-FEM may depend on the problem. The computed transfer functions were converted to impulse responses using discrete inverse Fourier transformation after multiplying the frequency characteristic of the source signal used for time-domain simulation.

Table 4 Locations of eight receivers (R1–R8).

Receiver	(x, y, z)	Receiver	(x, y, z)
R1	(0.7, 1.45, 1.2)	R5	(2.8, 1.45, 1.2)
R2	(0.7, 2.35, 1.2)	R6	(2.8, 2.35, 1.2)
R3	(0.7, 3.25, 1.2)	R7	(2.8, 3.25, 1.2)
R4	(0.7, 4.15, 1.2)	R8	(2.8, 4.15, 1.2)

4.2. Measuring Accuracy and Efficiency

Next, we evaluate the accuracies of Schemes 1 and 2 in frequency and time domains in terms of different aspects. We use the FD-FEM with PARDISO as a reference solution because sparse direct solvers produce a more accurate solution than iterative solvers do. In the frequency domain, the absolute error in the sound pressure level (SPL) between the two proposed schemes and the FD-FEM is computed as

$$e_{\mathrm{SPL}}(f_c) = \frac{1}{N_R}\sum_{i=1}^{N_R} |L_{\mathrm{FD}}(f_c, \boldsymbol{r}_i) - L_{\mathrm{TD}}(f_c, \boldsymbol{r}_i)|, \quad (30)$$

where N_R represents the number of receiving points. $L_{\mathrm{FD}}(f_c, \boldsymbol{r}_i)$ and $L_{\mathrm{TD}}(f_c, \boldsymbol{r}_i)$ are respectively the 1/3 and 1/96 octave band levels at the i-th receiver position at center frequency f_c, as calculated respectively using FD-FEM and Schemes 1 and 2. Additionally, we calculate the frequency response assurance criterion (FRAC) [34], which is a similarity measure between two complex frequency responses. FRAC is defined as

$$\mathrm{FRAC} = \frac{\left|\sum_{i=f_l}^{f_u} \bar{p}_{\mathrm{FD}}(f_i, \boldsymbol{r}) \cdot p_{\mathrm{TD}}(f_i, \boldsymbol{r})\right|^2}{\left[\sum_{i=f_l}^{f_u} \bar{p}_{\mathrm{FD}}(f_i, \boldsymbol{r}) p_{\mathrm{FD}}(f_i, \boldsymbol{r})\right]\left[\sum_{i=f_l}^{f_u} \bar{p}_{\mathrm{TD}}(f_i, \boldsymbol{r}) p_{\mathrm{TD}}(f_i, \boldsymbol{r})\right]}, \quad (31)$$

where $p_{\mathrm{FD}}(f_i, \boldsymbol{r})$ and $p_{\mathrm{TD}}(f_i, \boldsymbol{r})$ are respectively the complex sound pressures at frequency f_i and receiver $\boldsymbol{r}$ calculated using FD-FEM and the proposed schemes. The overline means the complex conjugate. f_l and f_u are lower- and upper-limit frequencies of 80 Hz and 1.4 kHz, respectively. FRAC takes a value in the range of [0, 1]. A larger value represents a higher similarity.

In the time domain, from practical aspects, the relative or absolute errors in four room acoustic parameters (T_{20}, EDT, C_{50}, and G) between the two proposed schemes and the FD-FEM were assessed respectively as

$$e_{\mathrm{T20}}(f_\mathrm{c}) = \frac{1}{N_\mathrm{R}} \sum_{i=1}^{N_\mathrm{R}} \frac{|T_\mathrm{FD}(f_\mathrm{c}, \boldsymbol{r}_i) - T_\mathrm{TD}(f_\mathrm{c}, \boldsymbol{r}_i)|}{T_\mathrm{FD}(f_\mathrm{c}, \boldsymbol{r}_i)}, \quad (32)$$

$$e_{\mathrm{EDT}}(f_\mathrm{c}) = \frac{1}{N_\mathrm{R}} \sum_{i=1}^{N_\mathrm{R}} \frac{|EDT_\mathrm{FD}(f_\mathrm{c}, \boldsymbol{r}_i) - EDT_\mathrm{TD}(f_\mathrm{c}, \boldsymbol{r}_i)|}{EDT_\mathrm{FD}(f_\mathrm{c}, \boldsymbol{r}_i)}, \quad (33)$$

$$e_{\mathrm{C50}}(f_\mathrm{c}) = \frac{1}{N_\mathrm{R}} \sum_{i=1}^{N_\mathrm{R}} |C_\mathrm{FD}(f_\mathrm{c}, \boldsymbol{r}_i) - C_\mathrm{TD}(f_\mathrm{c}, \boldsymbol{r}_i)|, \quad (34)$$

$$e_{\mathrm{G}}(f_\mathrm{c}) = \frac{1}{N_\mathrm{R}} \sum_{i=1}^{N_\mathrm{R}} |G_\mathrm{FD}(f_\mathrm{c}, \boldsymbol{r}_i) - G_\mathrm{TD}(f_\mathrm{c}, \boldsymbol{r}_i)|, \quad (35)$$

where $T_\mathrm{FD}(f_\mathrm{c}, \boldsymbol{r}_i)$, $EDT_\mathrm{FD}(f_\mathrm{c}, \boldsymbol{r}_i)$, $C_\mathrm{FD}(f_\mathrm{c}, \boldsymbol{r}_i)$, and $G_\mathrm{FD}(f_\mathrm{c}, \boldsymbol{r}_i)$ respectively denote T_{20}, EDT, C_{50}, and G at central frequency f_c and the i-th receiver position, calculated using FD-FEM. $T_\mathrm{TD}(f_\mathrm{c}, \boldsymbol{r}_i)$, $EDT_\mathrm{TD}(f_\mathrm{c}, \boldsymbol{r}_i)$, $C_\mathrm{TD}(f_\mathrm{c}, \boldsymbol{r}_i)$, and $G_\mathrm{TD}(f_\mathrm{c}, \boldsymbol{r}_i)$ are assessed using the proposed schemes.

The computational efficiency was evaluated by comparing the required memories and the computational times between the two proposed schemes and the FD-FEM. Note that Scheme 1 has an additional matrix-vector product in the third term on the right-hand side of Eq. (15) compared with Scheme 2, but our implementation realizes an efficient computation of this term by performing the computation only on the degrees of freedom related to MPPs. The degrees of freedom relevant to MPPs is lower than 0.5% of those in the entire system, indicating that the additional computational costs associated with extended-reaction MPP absorber modeling are not expensive. Additionally, computation times were evaluated in the frequency range of 1 Hz to 1.4 kHz for FD-FEM.

4.3. Results

First, Figs. 7 and 8 show SPLs at R1 for FD-FEM, Scheme 1, and Scheme 2 with MPP 1 and MPP 2, respectively. The two proposed schemes agree well with the FD-FEM results at all frequencies in both cases. For quantitative evaluation, Fig. 9 shows e_SPL values at the 1/3 and 1/96 octave band levels in the cases with MPP 1 and MPP 2. The two schemes show errors of less than 1 dB, except for the 1/96 octave band level for MPP 2 at frequencies lower than 110 Hz. The slightly large error at

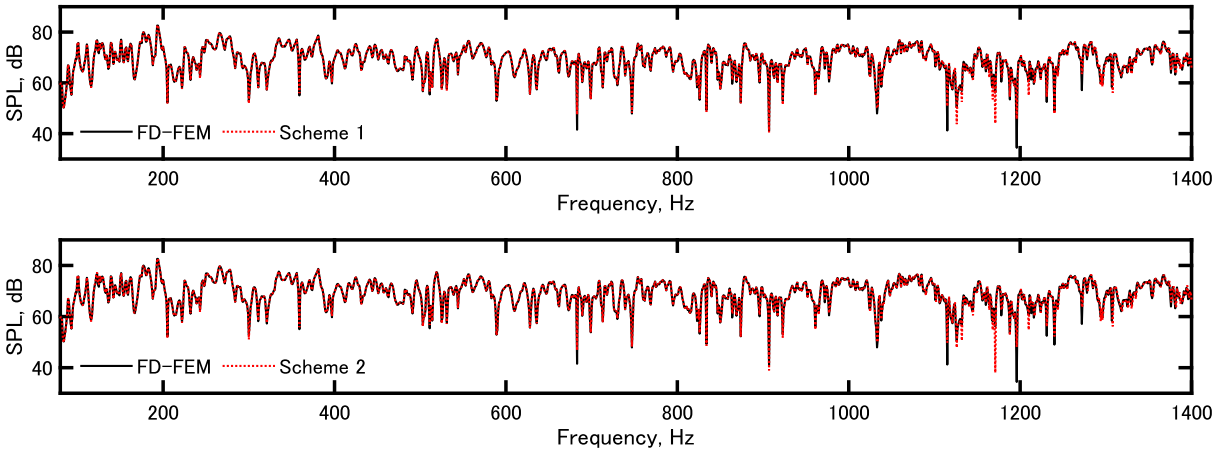

Fig. 7 SPLs at R1 in the meeting room with MPP 1: FD-FEM vs. Scheme 1 (upper); FD-FEM vs. Scheme 2 (lower).

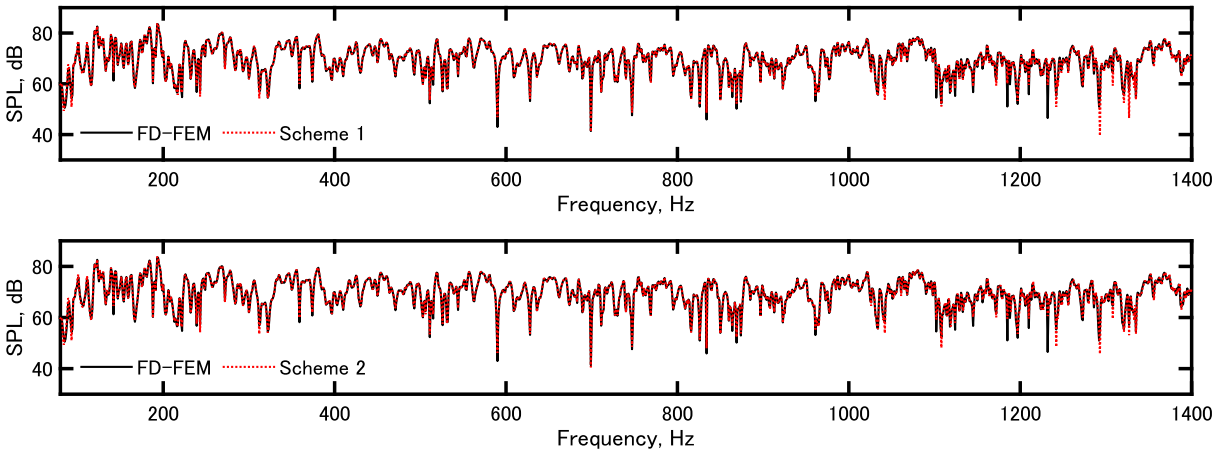

Fig. 8 SPLs at R1 in the meeting room with MPP 2: FD-FEM vs. Scheme 1 (upper); FD-FEM vs. Scheme 2 (lower).

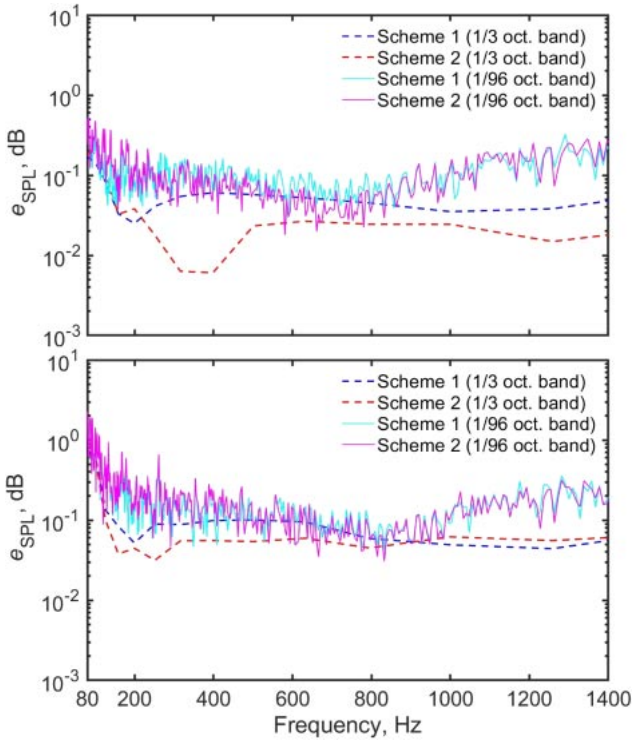

Fig. 9 e_{SPL} values at 1/3 and 1/96 octave band levels in cases with MPP 1 (upper) and MPP 2 (lower).

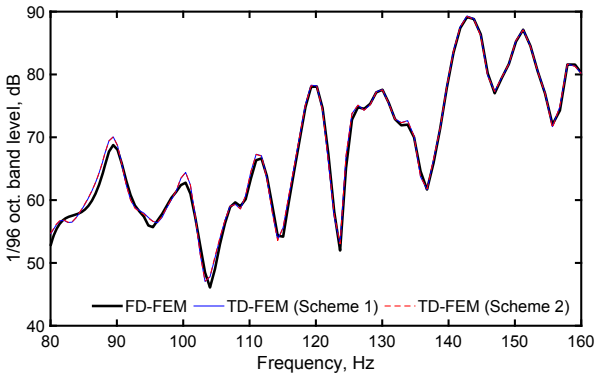

Fig. 10 Details of 1/96 octave band levels at R1 calculated using FD-FEM, Scheme 1, and Scheme 2.

Table 5 Relative error e_{T20} values [%] of Schemes 1 and 2 in cases with MPP 1 and MPP 2.

f_c, Hz	MPP 1		MPP 2	
	Scheme 1	Scheme 2	Scheme 1	Scheme 2
125	1.07	1.56	3.38	2.90
250	0.49	0.39	3.65	2.53
500	0.47	0.48	3.50	3.31
1,000	1.49	1.34	2.98	2.86

Table 6 Relative error e_{EDT} values [%] of Schemes 1 and 2 in cases with MPP 1 and MPP 2.

f_c, Hz	MPP 1		MPP 2	
	Scheme 1	Scheme 2	Scheme 1	Scheme 2
125	0.88	0.61	2.60	1.63
250	0.97	0.58	1.71	0.75
500	0.36	0.24	1.80	1.35
1,000	5.04	3.96	5.00	4.48

Table 7 Absolute error e_{C50} values [dB] of Schemes 1 and 2 in cases with MPP 1 and MPP 2.

f_c, Hz	MPP 1		MPP 2	
	Scheme 1	Scheme 2	Scheme 1	Scheme 2
125	0.06	0.08	0.12	0.08
250	0.03	0.04	0.06	0.03
500	0.04	0.02	0.12	0.08
1,000	0.11	0.08	0.18	0.16

Table 8 Absolute error e_G values [dB] of Schemes 1 and 2 in cases with MPP 1 and MPP 2.

f_c, Hz	MPP 1		MPP 2	
	Scheme 1	Scheme 2	Scheme 1	Scheme 2
125	0.06	0.04	0.13	0.08
250	0.04	0.02	0.07	0.03
500	0.05	0.02	0.09	0.05
1,000	0.04	0.02	0.05	0.05

low frequencies is attributable to the inadequate rational function approximation of Y_M and Y_{LM}, as presented in Fig. 1. Figure 10 shows how this inadequate approximation leads to effects at the 1/96 octave band level at receiver R1 in the case with MPP 2. Results show that the two proposed schemes slightly overestimate the peaks of SPL compared with the FD-FEM result. This meeting room problem has little absorption at all boundaries at low frequencies. Consequently, a slight error in the rational function approximation results is apparent in those visible differences for SPL. The values of the similarity measure FRAC were also larger than 0.99 at all receivers for both schemes. These results clearly indicate that the two proposed schemes can produce almost the same frequency response as FD-FEM.

Tables 5–8 respectively show errors in the four room acoustics parameters e_{T20}, e_{EDT}, e_{C50}, and e_G in Schemes 1 and 2 in cases with MPP 1 and MPP 2. Except for the relative error e_{EDT} at 1 kHz of Scheme 1, all errors in both schemes were smaller than the just notable differences (JNDs) of each parameter (5% for reverberation parameters [35], 1.1 dB for C_{50} [36] and 1 dB for G [35]). Those results demonstrate the excellent capability of the proposed schemes for room acoustics modeling, including extended-reacting MPP sound absorbers. These results also

Table 9 Computational costs for each FEM method in cases with MPP 1 and MPP 2: required memory (RM) in Mbytes; and computational time (CT) in s.

Method	RM, MBytes		CT, s	
	MPP 1	MPP 2	MPP 1	MPP 2
FD-FEM(PARDISO)	17,003	17,003	61,484	63,005
FD-FEM(CSQMOR)	391	391	42,616	42,981
Scheme 1	510	510	142	158
Scheme 2	510	510	139	145

indicate that the slightly large errors at the 1/96 octave band level at low frequencies in the case with MPP 2 have only a small effect on room acoustic parameters.

Finally, we show the computational efficiencies of the two proposed schemes relative to that of FD-FEM with two linear system solvers in Table 9. The two schemes show the same memory consumption of 1/33.3 times smaller than that of FD-FEM with PARDISO and 1.3 times larger than that of FD-FEM with CSQMOR. FD-FEM with CSQMOR exhibits the best performance in terms of memory requirements. However, it can be said that the two proposed schemes have attractive memory capabilities even though the rational function form of the MPP transfer admittance requires more than ten real poles. In fact, the two proposed schemes show remarkable computational speed compared with FD-FEMs with two linear system solvers. Schemes 1 and 2 respectively show 398–433 and 435–442 times shorter computational times than that of FD-FEM using PARDISO. Moreover, they are 272–300 and 296–306 times shorter than the FD-FEM using CSQMOR. This notable performance was observed in earlier work [6] in the case without the present extended-reaction MPP absorber model. Our formulation does not pose any computational inefficiency with the present model. Compared with Scheme 1, Scheme 2 shows a slightly high computational speed owing to few matrix-vector products, as described earlier. Note that the computational times of the two proposed schemes were about two minutes, indicating their high practicality in room-acoustics simulation.

5. CONCLUSION

We proposed two novel implicit TD-FEM schemes, Schemes 1 and 2, to address the ER of MPP sound absorbers for room-acoustics modeling. They are general formulations. Any finite element is applicable. Furthermore, the proposed schemes are the time-domain counterparts of our previous frequency-domain formulation [16]. In the two proposed schemes, an MPP leaf is modeled as an interior impedance boundary condition useful for considering the frequency-dependent transfer impedance of a rigid or limp MPP. However, note that various transfer impedance models of MPPs are potentially available. The convolution that appeared in the interior impedance boundary conditions is addressed efficiently by the ADE method. High stability is realized using an unconditionally stable Crank–Nicolson solver. After presenting a detailed formulation of the present schemes, their validity was demonstrated by comparing the sound absorption characteristics of four single-leaf MPP absorbers computed using the proposed schemes and theoretical TMM. Results revealed that, although the two proposed schemes can fundamentally capture the sound absorption characteristics of MPP absorbers, an error trend of a slight discrepancy of the reflection coefficient was observed around the resonant frequency. The error originates from the rational function approximation model. Therefore, for future work, developing a more precise fitting technique for the rational function approximation of the transfer admittance of MPP or examining other transfer impedance models of MPPs is expected to be necessary.

The performance characteristics of the proposed schemes compared with existing FD-FEMs with two linear equation solvers were examined in a real-scale meeting-room acoustics problem. Results indicated that the proposed schemes have accuracies comparable to those of the FD-FEMs, and that the schemes have significantly higher efficiencies with increase in computational speed of more than $\mathcal{O}(100)$ times. Regarding the performance of the two schemes in terms of accuracy and efficiency, Scheme 2 outperformed Scheme 1 with slightly higher performance. Scheme 2 enabled 296–442 times faster computation than FD-FEM while maintaining accuracy. To conclude, the proposed schemes were demonstrated to have high potential as attractive alternatives for room-acoustics simulation including extended-reacting MPP sound absorbers.

ACKNOWLEDGMENTS

This work was supported in part by a Kajima Foundation Scientific Research Grant and the Ono Charitable Trust for Acoustics.

REFERENCES

[1] F. Pind, A. P. Engsig-Karup, C. H. Jeong, J. S. Hesthaven, M. S. Mejling and J. Strømann-Anderson, "Time domain room acoustic simulations using the spectral element method," *J. Acoust. Soc. Am.*, **145**, 3299–3310 (2019).

[2] H. Wang and M. Hornikx, "Time-domain impedance boundary condition modeling with the discontinuous Galerkin method for room acoustics simulations," *J. Acoust. Soc. Am.*, **147**, 2534–2546 (2020).

[3] T. Yoshida, T. Okuzono and K. Sakagami, "Implementation of a frequency-dependent impedance boundary model into a room acoustic solver with time-domain finite element method," *Acoust. Sci. & Tech.*, **41**, 819–822 (2020).

[4] T. Okuzono, T. Yoshida and K. Sakagami, "Efficiency of room acoustic simulations with time-domain FEM including frequency-dependent absorbing boundary conditions: Comparison

with frequency-domain FEM," *Appl. Acoust.*, **182**, 108212 (2021).
[5] T. Yoshida, T. Okuzono and K. Sakagami, "Parallel dissipation-free and dispersion-optimized explicit time-domain FEM for large-scale room acoustics simulation," *Buildings*, **12**, 105 (2022).
[6] T. Okuzono and T. Yoshida, "High potential of small-room acoustic modeling with 3D time-domain finite element method," *Front. Built Environ.*, **8** (2022).
[7] T. Yoshida, T. Okuzono and K. Sakagami, "Binaural auralization of room acoustics with a highly scalable wave-based acoustics simulation," *Appl. Sci.*, **13**(5), 2832 (2023).
[8] A. Craggs, "A finite element model for rigid porous absorbing materials," *J. Sound Vib.*, **61**, 101–111 (1978).
[9] A. Craggs, "Coupling of finite element acoustic absorption models," *J. Sound Vib.*, **66**, 605–613 (1979).
[10] V. Easwaran and M. L. Munjal, "Finite element analysis of wedges used in anechoic chambers," *J. Sound Vib.*, **160**, 333–350 (1993).
[11] W. H. Chen, F. C. Lee and D. M. Chiang, "On the acoustic absorption of porous materials with different surface shapes and perforated plates," *J. Sound Vib.*, **237**, 337–355 (2000).
[12] R. Tomiku and T. Otsuru, "Sound fields analysis in an irregular-shaped reverberation room by finite element method," *J. Archit. Plann. Environ. Eng.*, **551**, 9–15 (2002) (in Japanese).
[13] M. Aretz and M. Vorländer, "Efficient modeling of absorbing boundaries in room acoustic FE simulations," *Acta Acust. united Ac.*, **96**, 1042–1050 (2010).
[14] T. Okuzono and K. Sakagami, "Dispersion error reduction of absorption finite elements based on equivalent fluid model," *Acoust. Sci. & Tech.*, **39**, 362–365 (2018).
[15] T. Sakuma, T. Iwase and M. Yasuoka, "Prediction of sound fields in rooms with membrane materials: Development of a limp membrane element in acoustical FEM analysis and its application," *J. Archit. Plann.* (*Trans. AIJ*), **63**(505), pp. 1–8 (1998).
[16] T. Okuzono and K. Sakagami, "A frequency domain finite element solver for acoustic simulations of 3D rooms with microperforated panel absorbers," *Appl. Acoust.*, **129**, 1–12 (2018).
[17] S. Mukae, T. Okuzono, K. Tamaru and K. Sakagami, "Modeling microperforated panels and permeable membranes for a room acoustic solver with plane-wave enriched FEM," *Appl. Acoust.*, **185**, 108383 (2022).
[18] T. Yoshida, T. Okuzono and K. Sakagami, "Time-domain finite element formulation of porous sound absorbers based on an equivalent fluid model," *Acoust. Sci. & Tech.*, **41**, 837–840 (2020).
[19] D. Dragna, P. Pineau and P. Blanc-Benon, "A generalized recursive convolution method for time-domain propagation in porous media," *J. Acoust. Soc. Am.*, **138**, 1030–1042 (2015).
[20] F. Pind, C. H. Jeong, A. P. Engsig-Karup, J. S. Hesthaven and J. Strømann-Anderson, "Time-domain room acoustic simulations with extended-reacting porous absorbers using the discontinuous Galerkin method," *J. Acoust. Soc. Am.*, **148**, 2851–2863 (2020).
[21] H. Wang and M. Hornikx, "Extended reacting boundary modeling of porous materials with thin coverings for time-domain room acoustic simulations," *J. Sound Vib.*, **548**, 117550 (2023).
[22] T. Okuzono, N. Shimizu and K. Sakagami, "Predicting absorption characteristics of single-leaf permeable membrane absorbers using finite element method in a time domain," *Appl. Acoust.*, **151**, 172–182 (2019).
[23] T. Yoshida, T. Okuzono and K. Sakagami, "Locally implicit time-domain finite element method for sound field analysis including permeable membrane sound absorbers," *Acoust. Sci. & Tech.*, **41**, 689–692 (2020).
[24] F. Pind, C. H. Jeong, J. S. Hesthaven, A. P. Engsig-Karup and J. Strømann-Anderson, "A phenomenological extended-reaction boundary model for time-domain wave-based acoustic simulations under sparse reflection conditions using a wave splitting method," *Appl. Acoust.*, **172**(4), 107596 (2021).
[25] K. Sakagami, M. Morimoto and M. Yairi, "A note on the effect of vibration of a microperforated panel on its sound absorption characteristics," *Acoust. Sci. & Tech.*, **26**, 204–207 (2005).
[26] D.-M. Maa, "Microperforated-panel wideband absorbers," *Noise Control Eng. J.*, **29**, 77–84 (1987).
[27] B. Yue and M. N. Guddati, "Dispersion-reducing finite elements for transient acoustics," *J. Acoust. Soc. Am.*, **118**, 2132–2141 (2005).
[28] J. F. Allard and N. Atalla, "Modeling multilayered systems with porous materials using the transfer matrix method," in *Propagation of Sound in Porous Media: Modeling Sound Absorbing Materials*, 2nd ed. (John Wiley & Sons, Chichester, 2009), Chap. 11, pp. 243–281.
[29] B. Gustavsen and A. Semlyen, "Rational approximation of frequency domain responses by vector fitting," *IEEE Trans. Power Deliv.*, **14**, 1052–1061 (1999).
[30] B. Gustavsen, "Fast passivity enforcement for pole-residue models by perturbation of residue matrix eigenvalues," *IEEE Trans. Power Deliv.*, **23**, 2278–2285 (2008).
[31] ISO 10534–2:1998, "Acoustics — Determination of sound absorption coefficient and impedance in impedance tubes — Part 2: Transfer-function method," International Organisation for Standardisation, Geneva, Switzerland (1998).
[32] Y. Miki, "Acoustical properties of porous materials — Modification of Delany–Bazley models —," *J. Acoust. Soc. Jpn.* (*E*), **11**, 19–24 (1990).
[33] J. Zhang and H. Dai, "A new quasi-minimal residual method based on a biconjugate *A*-orthonormalization procedure and coupled two-term recurrences," *Numer. Algorithms*, **70**, 875–896 (2015).
[34] D. Lee, T. S. Ahn and H. S. Kim, "A metric on the similarity between two frequency response functions," *J. Sound Vib.*, **436**, 32–45 (2018).
[35] ISO 3382–1:2009, "Acoustics — Measurement of the reverberation time of rooms related to other acoustical parameters," International Organisation for Standardisation, Geneva, Switzerland (2009).
[36] J. S. Bradley, R. Reich and S. G. Norcross, "A just noticeable difference in C_{50} for speech," *Appl. Acoust.*, **58**, 99–108 (1999).